

## Full length article

Atomic-scale observation and analysis of chemical ordering in  $M_3B_2$  and  $M_5B_3$  borides

X.B. Hu<sup>a, b, 1</sup>, H.Y. Niu<sup>c, 1</sup>, X.L. Ma<sup>a, d, \*</sup>, A.R. Oganov<sup>c, e, f, g, \*\*</sup>, C.A.J. Fisher<sup>b</sup>, N.C. Sheng<sup>h</sup>, J.D. Liu<sup>h</sup>, T. Jin<sup>h</sup>, X.F. Sun<sup>h</sup>, J.F. Liu<sup>a</sup>, Y. Ikuhara<sup>b, i, \*\*\*</sup>

<sup>a</sup> Shenyang National Laboratory for Materials Science, Institute of Metal Research, Chinese Academy of Sciences, Shenyang 110016, China

<sup>b</sup> Nanostructures Research Laboratory, Japan Fine Ceramics Center, Nagoya 456-8587, Japan

<sup>c</sup> Department of Geosciences, Center for Materials by Design, Institute for Advanced Computational Science, State University of New York, Stony Brook, NY 11794, USA

<sup>d</sup> School of Materials Science and Engineering, Lanzhou University of Technology, Lanzhou 730050, China

<sup>e</sup> Skolkovo Institute of Science and Technology, Skolkovo Innovation Center, 5 Nobel Street, Moscow 143026, Russia

<sup>f</sup> International Center for Materials Discovery, School of Materials Science and Engineering, Northwestern Polytechnical University, Xi'an 710072, China

<sup>g</sup> Moscow Institute of Physics and Technology, Dolgoprudny, Moscow Region 141700, Russia

<sup>h</sup> Superalloys Division, Institute of Metal Research, Chinese Academy of Sciences, Shenyang 110016, China

<sup>i</sup> Institute of Engineering Innovation, The University of Tokyo, Tokyo 113-8586, Japan

## ARTICLE INFO

## Article history:

Received 26 January 2018

Received in revised form

22 February 2018

Accepted 26 February 2018

Available online 3 March 2018

## Keywords:

Transient liquid phase (TLP) bonding

$M_3B_2$  and  $M_5B_3$  borides

Chemical ordering

Energy-dispersive X-ray spectroscopy (EDS)

Crystal structure prediction (CSP)

## ABSTRACT

Secondary phases precipitated in diffusion affected zones (DAZs) of a transient liquid phase (TLP) bonded Ni-based superalloy have a large impact on materials properties. Here we report an atomic-scale analysis of the crystal structures and elemental distributions within DAZ precipitates in a TLP-bonded single-crystal superalloy using a range of electron microscopy techniques. The predominant precipitate phases are found to be  $M_3B_2$ - and  $M_5B_3$ -type borides, where M is a mixture of transition metal elements. Atomically-resolved energy-dispersive X-ray spectroscopy in an aberration-corrected scanning transmission electron microscope (STEM) enabled the distributions of metal atoms within the precipitates to be determined. The observation that different metals occupy preferred sites within the crystals indicates that these phases are not uniform solid solutions, but instead are chemically ordered. Both borides contain two distinct metal lattice sites such that the phases can be described as  $L_2SB_2$  and  $L_4SB_3$ , where L and S are elements with larger (e.g., W, Mo) and smaller (e.g., Cr, Co, Ni) atomic numbers, respectively. Ordering of W and Cr is found to be particularly strong. A systematic search for stable phases within the chemical space of the W–Cr–B ternary system using the crystal structure prediction (CSP) program USPEX provided further insights into the nature of the observed chemical ordering. This combination of STEM and CSP techniques provides a direct and robust way of determining chemical features and local structures of multicomponent phases with atomic resolution even when particle sizes are too small for analysis using conventional methods.

© 2018 Acta Materialia Inc. Published by Elsevier Ltd. All rights reserved.

\* Corresponding author. Shenyang National Laboratory for Materials Science, Institute of Metal Research, Chinese Academy of Sciences, Shenyang 110016, China.

\*\* Corresponding author. Department of Geosciences, Center for Materials by Design, Institute for Advanced Computational Science, State University of New York, Stony Brook, NY 11794, USA.

\*\*\* Corresponding author. Nanostructures Research Laboratory, Japan Fine Ceramics Center, Nagoya 456-8587, Japan.

E-mail addresses: [xlma@imr.ac.cn](mailto:xlma@imr.ac.cn) (X.L. Ma), [artem.oganov@stonybrook.edu](mailto:artem.oganov@stonybrook.edu) (A.R. Oganov), [ikuahara@sigma.t.u-tokyo.ac.jp](mailto:ikuahara@sigma.t.u-tokyo.ac.jp) (Y. Ikuhara).

<sup>1</sup> These authors contributed equally to this work.

## 1. Introduction

Because of its beneficial effect in strengthening grain boundaries, boron is widely used as a micro-alloying element in superalloys to improve their mechanical properties, particularly creep performance [1–4]. Boron exhibits low solubility ( $\approx 100$  ppm) in the bulk of the superalloys, and prior studies have suggested that it prefers to reside at grain boundaries [4–6]. Recent work has shown that it forms various kinds of borides with different transition metal elements [7–10], and in addition to precipitating at grain boundaries, precipitation within grains also occurs [11,12]. Boron is also

considered to be an important melting point depressant because it forms a eutectic with Ni, and it is widely used as the filler material in transient liquid phase (TLP) bonding, an advanced welding technique for joining advanced engineering alloys such as superalloys [13]. During TLP bonding, a large number of boride precipitates form in the diffusion affected zone (DAZ) near the joint, which has a strong effect on the mechanical properties of the bonded material [14,15]. Better understanding of the microstructural characteristics and compositions of these boride precipitates is an important step in optimizing the TLP bonding process and thereby improving the integrity of superalloy components.

In general, four types of borides have been reported to form in Ni-based superalloys, viz.,  $M_3B_2$ -,  $M_5B_3$ -,  $M_2B$ -, and  $M_{23}B_6$ -type borides [16–18], where M is a combination of transition metal elements. Of these phases,  $M_3B_2$  and  $M_5B_3$  are the most commonly observed. Although the average crystal structures of  $M_3B_2$  and  $M_5B_3$  have been determined using a number of techniques, there is still uncertainty about how the transition metals are distributed across crystallographically distinct lattice sites, i.e., whether they are distributed randomly over different sites or if they preferentially occupy sites depending on their chemistry or atomic sizes.

Based on X-ray diffraction analysis, Beattie proposed that ordering of metal atoms occurs in  $M_3B_2$  borides [19]. In the case of the  $M_5B_3$  phase, however, the transition metal elements are still generally thought to be distributed randomly over the M sublattice. Although X-ray diffraction (both conventional and synchrotron) and neutron diffraction are powerful tools for determining structures and site occupancy factors when combined with Rietveld refinement methods, the results pertain only to the average structure. Combined with the fact that many types of precipitates can coexist in the same alloy, structure refinement of individual phases with complicated composition features remains a daunting task that requires state-of-the-art characterization methods.

Atom probe tomography (APT) is another powerful technique for obtaining useful chemical insights with higher spatial resolution [6,8,10,20]. However, although it is possible to attain spatial depth resolutions within a few tens of picometers, lateral resolutions are intrinsically limited to a fraction of a nanometer, which generally precludes full reconstruction of a precipitate's crystal structure [21]. The crystallographic information retrieved from APT enables individual crystal planes to be resolved and precise site occupancies to be determined [22], but to date such detailed analysis has only been carried out successfully in the case of the  $L1_2$  ordered  $\gamma'$  phase, which has a simple crystal lattice [23,24].

In general, accurate determination of the real-space distribution of different metal atoms in precipitates with a complicated structural and chemical makeup requires use of alternative techniques to those described above. One such technique is scanning transmission electron microscopy (STEM), which has a very high spatial resolution and can be used to examine much smaller regions within the materials. In previous work, we used this method to analyze boride precipitates and concluded that occupational ordering indeed occurs in both  $M_3B_2$  and  $M_5B_3$  [25], although a quantitative analysis of site occupancies was not undertaken at that time. Since the development of aberration correctors, atomic-resolution electron energy loss spectroscopy (EELS) and energy dispersive spectroscopy (EDS) have emerged as powerful techniques for chemical analysis of a wide range of materials [26–29]. Of these two techniques, atomic-resolution EDS mapping is more robust in detecting heavy elements because of the intrinsically low-scattering cross-section of electrons with higher energy loss [30–32].

In this study we use atomic-resolution EDS to obtain real-space maps of different metallic elements in  $M_3B_2$  and  $M_5B_3$  borides precipitated in the DAZ of a TLP-bonded superalloy in order to quantify site occupancies within the two crystal lattices. The results

provide direct evidence that chemical ordering occurs in both of these borides. As Cr and W are the two major metallic elements in the boride precipitates, to better understand the ordering phenomenon we also carried out theoretical modeling of compounds in the W-Cr-B ternary system using a recently developed structure prediction method built upon the evolutionary algorithm USPEX [33–35].

## 2. Experimental methods

### 2.1. Preparation of bulk samples

Bulk samples used in this study were taken from a transient liquid phase (TLP) bonded superalloy. Bars of the superalloy with nominal composition (in at%) of 12.4 Al, 7.2 Co, 6.5 Cr, 1.8 W, 1.3 Ti, 0.7 Mo, and balance Ni were directionally solidified along the [001] direction using a high-rate solidification method using a spiral selector. Cylindrical bars 13 mm in diameter and 6 mm in height were cut from the as-cast bars. Next, an 8 mm × 300 mm gap parallel to the [001] direction of the single crystal was cut in the center of the cylinders. A filler alloy with nominal composition (in at%) of 14.4 Cr, 16.2 B, and balance Ni was inserted into the gap. Details of the TLP bonding process can be found in our previous reports [13,36]. After bonding, several slices near the joint were cut perpendicular to one of the bonded interfaces for structural characterization.

### 2.2. Electron microscopy and image simulations

A Leica optical microscope and Oxford scanning electron microscope (SEM) were used to characterize the macro-morphological features. Electron transparent specimens were prepared by conventional mechanical polishing and Ar-ion beam milling. The thickness of the electron-transparent region used for high quality atomic resolution imaging was less than 100 nm, as determined using the EELS log-ratio technique [37].

Detailed TEM characterization was performed using a probe-corrected JEM-ARM200CF (JEOL, Co. Ltd) microscope equipped with two silicon drift detectors (SDDs). The operation voltage was 200 kV, and the probe-forming aperture semi-angle was approximately 25 mrad, which yielded a probe size of around 1.2 Å with a probe current of about 60 pA. The collection angle of the high angle annular dark field (HAADF) detector ranged from 50 to 200 mrad. The detector size for a single SDD was 100 mm<sup>2</sup> and the solid angle for the whole collection system was about 1.7 sr.

Atomic-resolution EDS mapping was performed using the NSS3 software developed by Thermo Fisher Scientific Inc. Atomic resolution HAADF image simulations were performed using the xHREM software package (HREM Research Inc.). The probe in the simulations was assumed to have an aberration-free Gaussian distribution with a half-width at half-maximum of 0.6 Å to account for the finite effective source. Structural models of  $M_3B_2$  and  $M_5B_3$  were constructed based on the crystal structures of binary  $V_3B_2$  and  $Cr_5B_3$  [38,39], details of which are provided in Table 1. The simulation employed Weickenmeier-Kohl scattering cross-sections including thermal diffuse scattering. Debye-Waller factors of W and Cr were set to 1, and the sample thickness was set at 20 nm. The convergence semi-angle and collection inner/outer semi-angles were the same as those used in scanning transmission electron microscopy (STEM) experiments.

### 2.3. Computational methods

Searches for stable compounds and structures within the Cr-B system were performed using the USPEX code [33–35], which

**Table 1**The structure type, space group, lattice parameters, Wyckoff positions, and fractional atomic coordinates of binary phases  $V_3B_2$  and  $Cr_3B_3$ .

Structure type (Strukturbericht symbol)	Space group (number)	Lattice parameters/Å	Atom (Wyckoff site)	Fractional coordinates		
				x	y	z
$V_3B_2$ ( $D5_a$ )	$P4/mbm$ (127)	$a = 5.76$ $c = 3.04$	V (4h)	0.173	0.673	0.500
			V (2a)	0.000	0.000	0.000
			B (4g)	0.388	0.888	0.000
$Cr_3B_3$ ( $D8_f$ )	$I4/mcm$ (140)	$a = 5.46$ $c = 10.64$	Cr (16l)	0.166	0.666	0.150
			Cr (4c)	0.000	0.000	0.000
			B (8h)	0.625	0.125	0.000
			B (4a)	0.000	0.000	0.250

utilizes an evolutionary algorithm to predict stable compounds and structures from the chemical elements alone. Its accuracy and reliability have been demonstrated for a range of different materials systems [40,41]. In this method, stable compositions are identified from a convex hull construction: a compound is considered thermodynamically stable if the enthalpy of its decomposition into any other compounds is positive. Structure relaxations were performed within the framework of density functional theory (DFT) using the Perdew-Burke-Ernzerhof (PBE) functional and the all-electron projector augmented wave (PAW) method, as implemented in the VASP code [42,43]. A plane-wave kinetic energy cutoff of 600 eV was used, and the Brillouin zone sampled with a resolution of  $2\pi \times 0.03 \text{ \AA}^{-1}$ , which resulted in excellent convergence of energy differences, stress tensors and structural parameters. The first generation of structures was created randomly.

All structures were relaxed at ambient pressure and 0 K and the calculated enthalpy was used to test the goodness of fit. The energetically highest 30% of structures was discarded and a new generation was created, 30% randomly and 70% from the lowest-enthalpy structures through heredity, lattice mutation, and transmutation (variable-composition search) or permutation (fixed-composition search). In addition, phonon dispersions throughout

the Brillouin zone of each compound were derived using the finite-displacement approach implemented in the Phonopy code [44]. Lattice dynamics calculations of all the low-enthalpy structures showed no imaginary vibration frequencies, suggesting they are dynamically stable over the pressure ranges considered here. The calculated bulk modulus ( $B$ ), shear modulus ( $G$ ), and Young's modulus ( $E$ ) of each phase were derived using Reuss-Voigt-Hill averages [45].

### 3. Results and discussion

#### 3.1. General structural features of $M_3B_2$ and $M_5B_3$

The optical micrograph in Fig. 1a shows the macrostructural features near the joint in the TLP bonded system used in this study. Based on knowledge of the bonding process and precipitation features [13], three characteristic regions were identified, namely the non-isothermal solidification zone (NSZ), isothermal solidification zone (ISZ), and diffusion affected zone (DAZ). The SEM micrograph in Fig. 1b obtained in back-scattered electron mode clearly reveals a large number of precipitates in the DAZ. In order to identify the structural features of these precipitates, TEM was

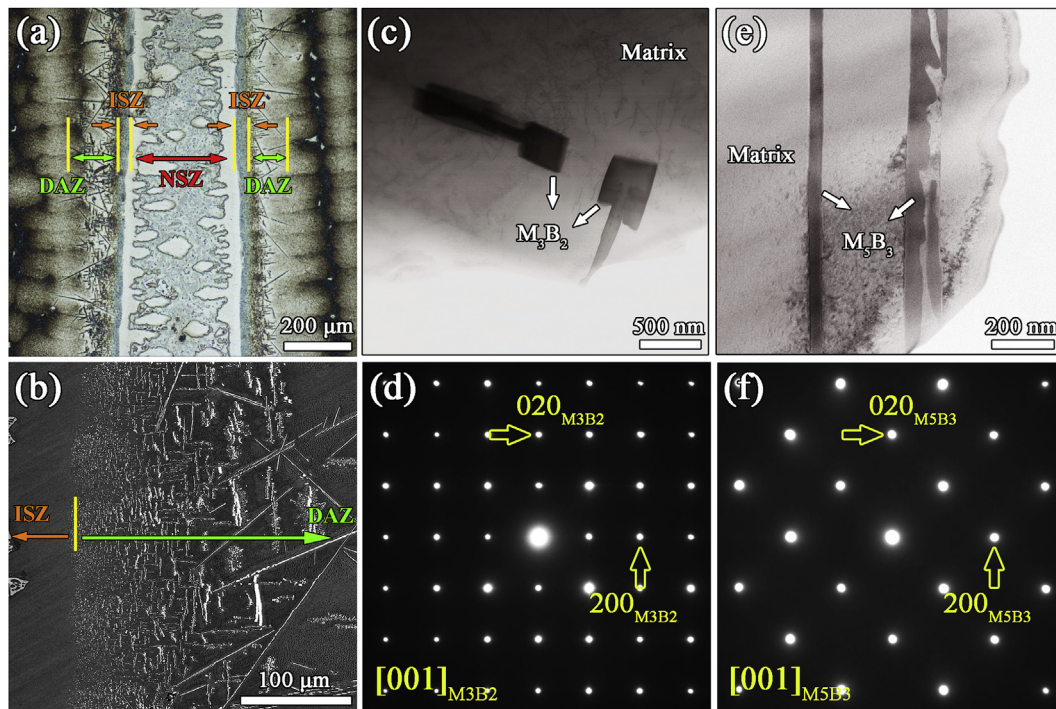


**Fig. 1.** (a) Optical micrograph and (b) SEM back-scattered electron micrograph showing the macro-morphological features of boride precipitates near the joint in a TLP-bonded superalloy. The approximate locations of the nonisothermal solidification zone (NSZ), isothermal solidification zone (ISZ), and diffusion affected zone (DAZ) are indicated. (c) and (d) BF-STEM images of intragranular boride precipitates  $M_3B_2$  and  $M_5B_3$ , respectively. (e) and (f) EDPs along [001] of  $M_3B_2$  and  $M_5B_3$  precipitates, respectively.

performed. The electron diffraction patterns (EDPs) in Fig. 1d and f were obtained from the precipitates in the grain interiors indicated in the bright field STEM (BF-STEM) images in Fig. 1c and e, respectively. By indexing these EDPs, the precipitates in Fig. 1c and e were identified as  $M_3B_2$ - and  $M_5B_3$ -type borides, respectively. These borides were found to be the main precipitates in the DAZ of the TLP bonded alloy used in this study.

The  $M_3B_2$ -type boride was determined to have the same crystal structure as  $V_3B_2$  with space group  $P4/mbm$  and Strukturbericht symbol  $D5_a$ . Its lattice parameters were measured to be  $a = 0.57$  nm and  $c = 0.30$  nm. Ideally, structural extinction resulting from the  $b$  glide being in the (100) plane means that only  $Ok$  reflections with  $k$  even should appear. However, because of dynamic scattering effects, all reflections appeared, as seen in Fig. 1d.

The  $M_5B_3$ -type boride was found to have the same crystal structure as  $Cr_5B_3$  with space group  $I4/mcm$  and Strukturbericht symbol  $D8_f$ . Its lattice parameters were measured to be  $a = 0.57$  nm and  $c = 1.04$  nm. Extinction of  $h00$  and  $k00$  reflections with  $h$  and  $k$  odd in Fig. 1f EDPs is consistent with it having a body-centered lattice.

### 3.2. Chemical ordering in $M_3B_2$ and $M_5B_3$

In order to detect any chemical ordering in the  $M_3B_2$  and  $M_5B_3$  precipitates, atomic resolution HAADF imaging in STEM mode was performed. HAADF STEM is a better choice for high resolution imaging than conventional transmission electron microscopy because HAADF images provide atomic number ( $Z$ ) contrast with intensities proportional to  $Z^{1.7-1.9}$  [46]. For the tetragonal structures of  $M_3B_2$  and  $M_5B_3$ , the best orientation for determining site occupancies of different metallic elements in both cases was determined to be [001], because each atom column along this direction contains only one type of Wyckoff site. In addition, atom columns are widely spaced when viewed along this direction. Any occupancy differences can thus be more easily distinguished in HAADF images viewed down this zone axis.

In the atomic-resolution HAADF image in Fig. 2a taken along the [001] direction of an  $M_3B_2$  precipitate, columns with two distinct levels of contrast are discernible. The bright columns are labelled '1', and correspond to  $4h$  sites in the  $D5_a$  lattice of the  $M_3B_2$  phase, while the dark columns, labelled '2', correspond to  $2a$  sites. The three-dimensional plot in Fig. 2b of the signal intensity as a function of position within the area enclosed by the square in Fig. 2a shows that the intensity from type 2 columns is less than half that of type 1 columns. As [001] columns in  $M_3B_2$  all have the same atom densities, the difference in contrast in Fig. 2a and b suggests preferential occupancy of different sites by metal atoms with different  $Z$  values. However, the intensity in HAADF images only reflects the average atomic number of that particular column, without providing any information about individual site occupancies.

To determine which types of atoms are in each column, we performed atomic-resolution EDS mapping on the region of crystal shown in Fig. 2a. Spectra from type 1 columns only, type 2 columns only, and all columns together are compared in Fig. 2c, where each profile is normalized to its W-M peak. The magnified view of the combined EDS profiles in the inset of Fig. 2c reveals that columns 2 are much richer in Cr, Ni, and Co than type 1 columns. Since all profiles are normalized to the W-M peak, enrichment of Cr, Ni, and Co in type 2 columns necessarily means a lower concentration of W and Mo compared to that in type 1 columns. A semi-quantitative analysis of all columns in the EDS profile indicates that the composition of the  $M_3B_2$  precipitate can be written (approximately) as  $(W_{0.3}Mo_{0.2}Cr_{0.3}Ni_{0.16}Co_{0.04})_3B_2$ . It should be noted that, due to delocalizing effects, EDS profiles of type 1 columns always contain some signals from type 2 columns (and vice versa), so EDS profiles of each column do not provide an absolutely accurate measure of the composition, and will tend to underestimate the differences between different column types. Nevertheless, any differences detected by this method can be taken as indicative of actual differences in the elemental makeup of the columns.

Atom-resolved EDS maps generated from individual element edges are shown in Fig. 3a–f. The EDS maps in Fig. 3a and b reveal

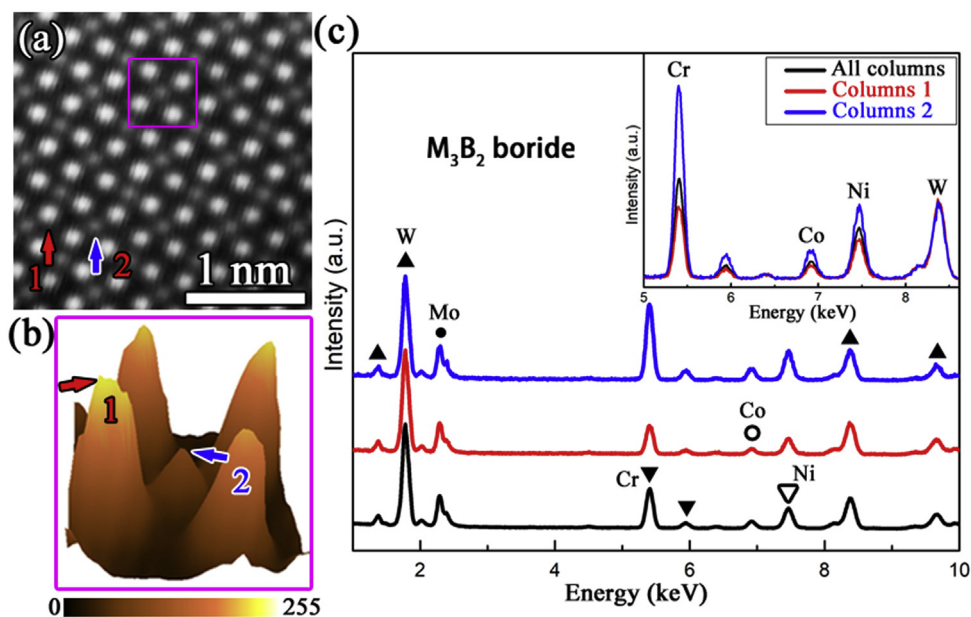


**Fig. 2.** (a) Atomic resolution HAADF image taken along [001] showing atom columns with two distinct contrast levels, labelled '1' and '2', in an  $M_3B_2$  precipitate. Type 1 and type 2 columns correspond to Wyckoff positions  $4h$  and  $2a$ , respectively, in space group  $P4/mbm$ . (b) A three-dimensional intensity map of the region enclosed by the mauve square in (a). The color bar indicates the intensity normalized to values between 0 and 255. (c) EDS profiles from the region in (a) using signals from type 1 and 2 columns, type 1 columns only (bright), and type 2 columns only (dark), with peaks from different metal elements as indicated. All profiles are normalized to the W-M peak. The inset shows a magnified view of all three profiles overlaid on one another. (For interpretation of the references to color in this figure legend, the reader is referred to the Web version of this article.)

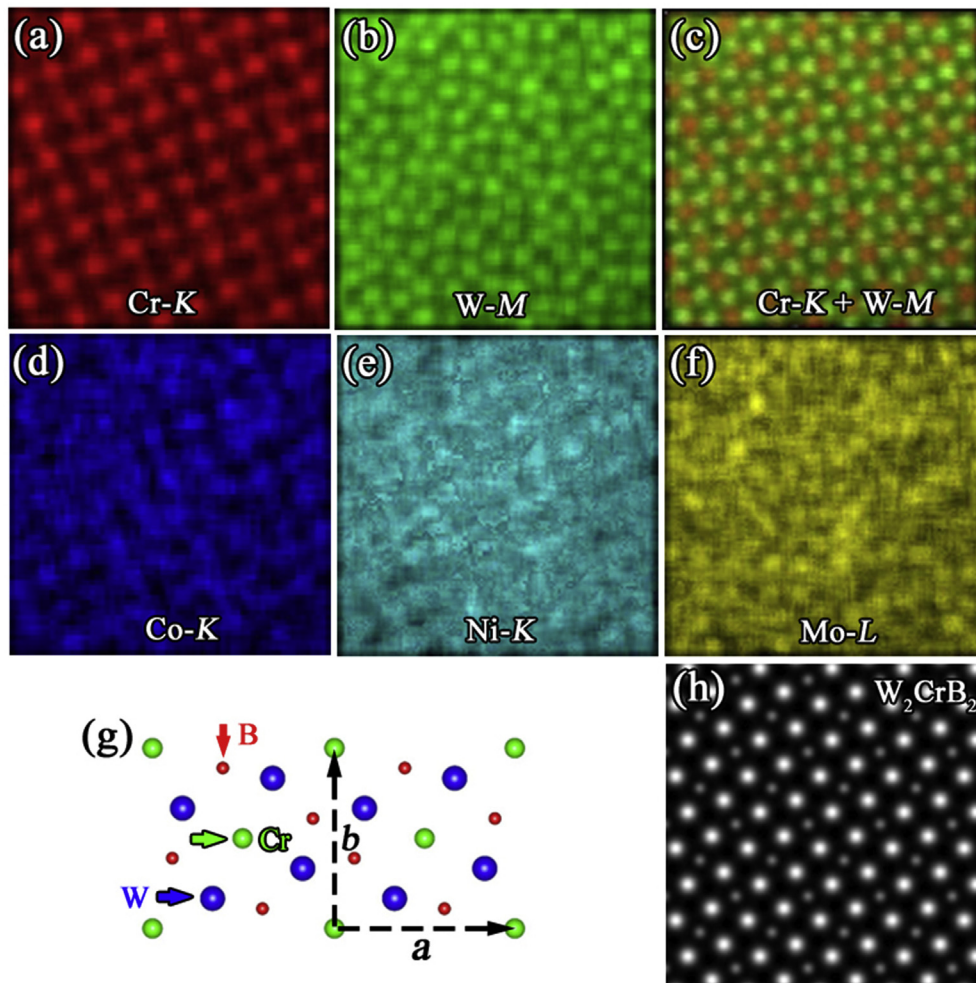


**Fig. 3.** (a–f) Atomic resolution EDS maps of the region in Fig. 2a generated using (a) Cr-K, (b) W-M, (c) Cr-K + W-M, (d) Co-K, (e) Ni-K, and (f) Mo-L peaks. (g) Projection of the ordered  $W_2CrB_2$  structure along [001]. The red, green, and blue balls represent B, Cr, and W atoms, respectively, with lattice vectors  $a$  and  $b$  indicated. (h) Simulated atomic resolution HAADF image along [001] using the model in (g). (For interpretation of the references to color in this figure legend, the reader is referred to the Web version of this article.)

the strong preferences of W and Cr to occupy different Wyckoff positions. This is more clearly seen in the combined map of Cr-K and W-M signals in Fig. 3c. The maps in Fig. 3d and e show that Co and Ni tend to prefer the same positions as Cr, although the ordering is not as strong as for Cr. This may partially be because of the low concentrations of Co and Ni in the precipitate compared with Cr. Of these three first-row transition metals, the strength of chemical ordering increases in the order  $Ni < Co < Cr$ , i.e., with increasing atom size.

Comparison of Fig. 3b and f reveals that Mo has a slight preference for the same sites as W, but that this is noticeably weaker than that of W. Considering that the concentration of Mo is comparable to that of W, this suggests that the tendency of Mo to order is weaker than that of W in the case of  $M_3B_2$ . Nevertheless, overall the results show that elements with larger  $Z$  (e.g., W and Mo) tend to prefer  $4h$  sites and elements with smaller  $Z$  (e.g., Cr, Co, and Ni) tend to prefer  $2a$  sites. The ordered form of  $M_3B_2$  can thus be described as  $L_2SB_2$ , where L and S represent elements with large  $Z$  (e.g., W, Mo) and small  $Z$  (e.g., Cr, Co, Ni), respectively.

To test the validity of these inferences, image simulations were performed using a simplified model of the  $M_3B_2$  precipitate in which W and Cr were the only metal atoms, i.e., a composition of  $W_2CrB_2$ , as these two elements exhibited the strongest

occupational ordering. The schematic in Fig. 3g shows a projection of the unit cell of  $W_2CrB_2$  down [001]. The atomic-resolution HAADF simulation image of this structure is shown in Fig. 3h. Comparison of Figs. 3h and 2a shows that the simulated image reproduces the experimentally observed contrast features well.

Fig. 4a shows an atomic-resolution HAADF image of an  $M_5B_3$  precipitate viewed along [001], in which two kinds of characteristic contrast spots, also labelled '1' (16l positions) and '2' (4c positions), can be distinguished. Type 1 columns are brighter than type 2 columns. This is more clearly seen in Fig. 4b, which is a three-dimensional plot of intensity as a function of position in the region enclosed by the square in Fig. 4a. Since the atom densities of type 1 columns and type 2 columns are the same along [001] in the  $D8_7$  lattice of  $M_5B_3$ , the contrast difference in Fig. 4a indicates preferential occupancy of the two sites by different metal atoms.

To determine the distributions of the metal atoms in real space, atomic-resolution EDS mapping was performed on the region in Fig. 4a in the same way as for the  $M_3B_2$  precipitate. Semi-quantitative analysis of the EDS profile from all columns visible in Fig. 4c indicates that the composition of the  $M_5B_3$  boride can be written (approximately) as  $(W_{0.33}Mo_{0.26}Cr_{0.31}Ni_{0.06}Co_{0.04})_5B_3$ . Comparison of the overlaid EDS profiles in the inset of Fig. 4c reveals that type 2 columns are slightly richer in Cr, Ni, and Co than

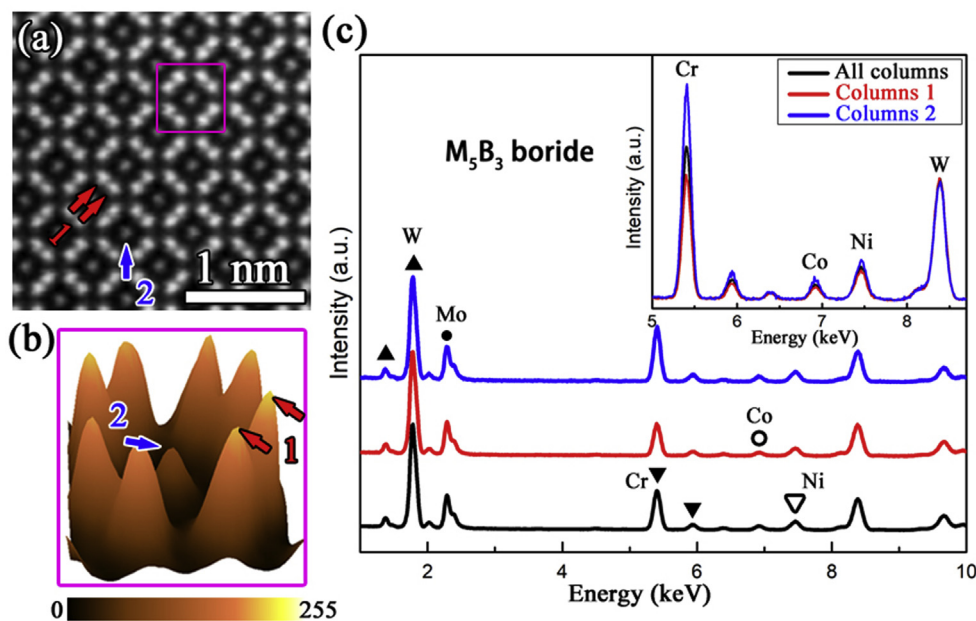


**Fig. 4.** (a) Atomic resolution HAADF image taken along [001] showing atom columns with two distinct contrast levels labelled '1' and '2', in an  $M_5B_3$  precipitate. Type 1 and type 2 columns correspond to Wyckoff positions  $16l$  and  $4c$ , respectively, in space group  $I4/mcm$ . (b) A three dimensional intensity map of the region enclosed by the mauve square in (a). The color bar indicates the intensity normalized to values between 0 and 255. (c) EDS profiles from the region in (a) using signals from type 1 and 2 columns, type 1 columns only (bright), and type 2 columns only (dark), with peaks from different metallic elements as indicated. All profiles are normalized to the W-M peak. The inset shows a magnified view of all three profiles overlaid on one another. (For interpretation of the references to color in this figure legend, the reader is referred to the Web version of this article.)

type 1 columns. Again because of delocalizing effects, the measured compositional difference between column types will be smaller than the actual difference.

Because all EDS profiles were normalized to the W-M peak, enrichment of Cr, Ni, and Co in type 2 columns means a lower concentration of W and Mo compared with type 1 columns. The individual atom-resolved EDS maps in Fig. 5a and b, and the combined map in Fig. 5c show that elements Cr and W preferentially occupy different Wyckoff positions in  $M_5B_3$ . Based on the element maps in Fig. 5d–f, Co, Ni and Mo appear to be distributed evenly over both site types. This is similar to the weak ordering tendencies of Co, Ni, and Mo in the  $M_3B_2$  precipitate. The ordered form of  $M_5B_3$  can be described as  $L_4SB_3$ , where L and S represent elements with larger (e.g., W) and smaller (e.g., Cr) atomic numbers, respectively. In the case of  $M_5B_3$ , however, Cr was also detected in columns 1, as indicated by arrows in Fig. 5a, and W in columns 2, as indicated by arrows in Fig. 5b, although at lower concentrations. This suggests that the tendency for heavier/larger atoms to order in  $M_5B_3$  is weaker than that in  $M_3B_2$ .

A simplified model of the ordered form of  $M_5B_3$  was constructed using W and Cr as the only metal atoms, as their occupational ordering was strongest, giving a composition of  $W_4CrB_3$ . A structural projection of  $W_4CrB_3$  along [001] is shown in Fig. 5g. The simulated atomic-resolution HAADF image of this structure down the same direction shown in Fig. 5h reproduces the experimentally observed contrast features well (see Fig. 4a), strongly suggesting that occupational ordering also occurs in  $M_5B_3$  precipitates.

To further confirm that the HAADF images correspond to a particular chemical ordering, we also generated simulated HAADF images of two other possible metal atom distributions, namely a structure model with W and Cr atoms distributed randomly over type 1 and 2 column sites, corresponding to  $(W,Cr)_3B_2$  and  $(W,Cr)_5B_3$ , and a model with the inverse ordering of metal atoms to those described above, i.e.,  $WCr_2B_2$  and  $WCr_4B_3$ . Disordered models were constructed with W:Cr ratios of 2:1 and 4:1 respectively.

Fig. 6a and b shows the structural projections of  $(W_{0.67}Cr_{0.33})_3B_2$  and  $WCr_2B_2$  along [001], respectively, and Fig. 6c and d shows projections of  $(W_{0.8}Cr_{0.2})_5B_3$  and  $WCr_4B_3$  structures along [001], respectively. The corresponding simulated HAADF images are shown in Fig. 6e, f, 6g, and 6h, respectively. The images for the randomly distributed atoms show uniform contrast for both types of columns. Comparing the simulated images in Fig. 6f and h with their respective counterparts in Figs. 3h and 5h shows that although both produce spots with two levels of contrast they form very different patterns, with the ratios of the number of brighter and darker columns inverted. The images in Figs. 3h and 5h best match the experimental images in Figs. 2a and 4a, confirming that these particles exhibit  $L_2SB_2$  and  $L_4SB_3$  type ordering, respectively. All other precipitates examined revealed the same types of ordering.

### 3.3. Theoretical prediction of stable phases in the W-Cr-B ternary system

Theoretical calculations of different structures and compositions within the ternary W-Cr-B system were performed using the crystal structure prediction method implemented in the USPEX code [33–35] to identify the main factors affecting structural stability and site preferences in the boride precipitates. Structure searches for composition  $W_2CrB_2$  indicated that the ground-state structure of  $W_2CrB_2$  is the same as that of  $V_3B_2$ , with Cr and W atoms on Wyckoff positions  $2a$  and  $4h$ , respectively, as given in Table 2. These results are in excellent agreement with our experimental observations, demonstrating the reliability of the structure prediction method. Using the same procedure, the ground-state structure of  $W_4CrB_3$ , summarized in Table 2, was predicted to be the same as that of  $Cr_5B_3$ , also in agreement with our experimental result. The ground-state structures for a range of W/Cr ratios and degrees of disorder were also investigated to better understand why experimentally ordered forms are richer in W than Cr.

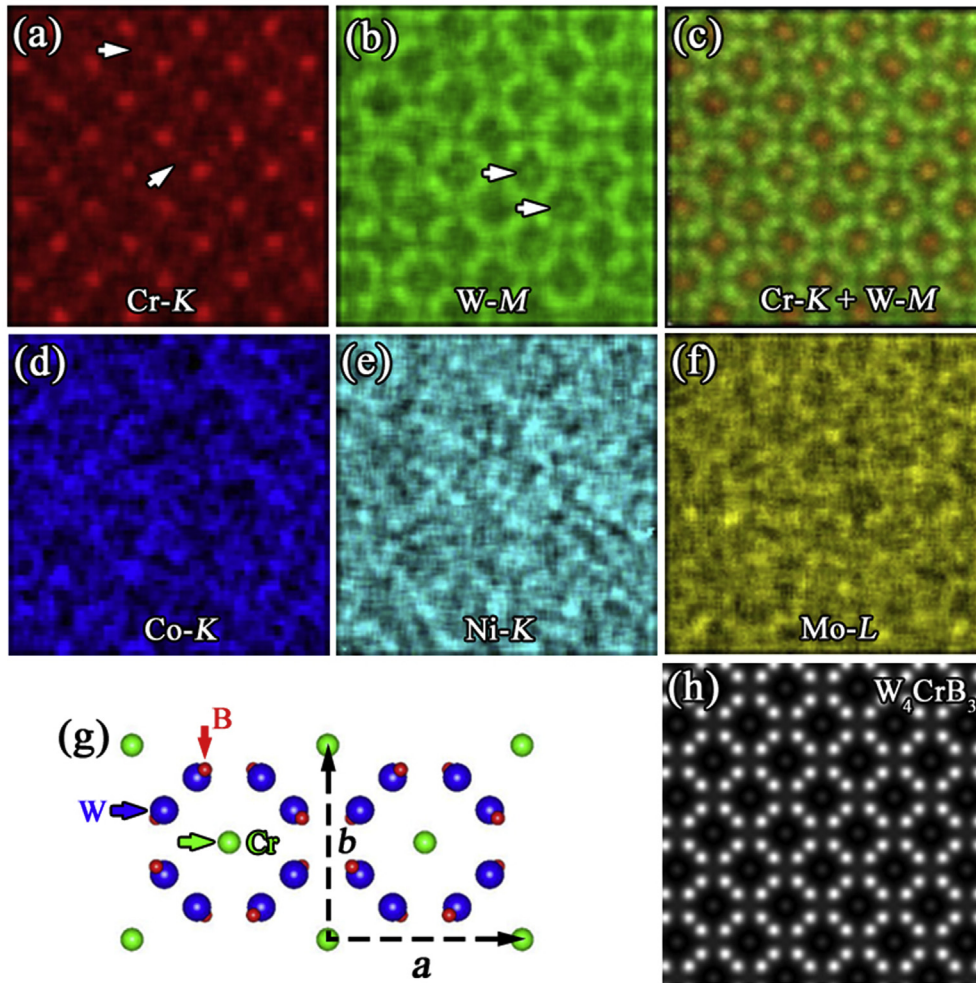


**Fig. 5.** (a–f) Atomic resolution EDS maps of the region in Fig. 4a generated using (a) Cr-K, (b) W-M, (c) Cr-K + W-M, (d) Co-K, (e) Ni-K, and (f) Mo-L peaks. The arrows in (a) indicate weak signals from Cr in type 1 columns. The arrows in (b) indicate weak signals from W in type 2 columns. (g) Projection of the ordered  $W_4CrB_3$  structure along [001]. The red, green, and blue balls represent B, Cr, and W atoms, respectively, with lattice vectors  $a$  and  $b$  indicated. (h) Simulated atomic resolution HAADF image along [001] using the model in (g). (For interpretation of the references to color in this figure legend, the reader is referred to the Web version of this article.)

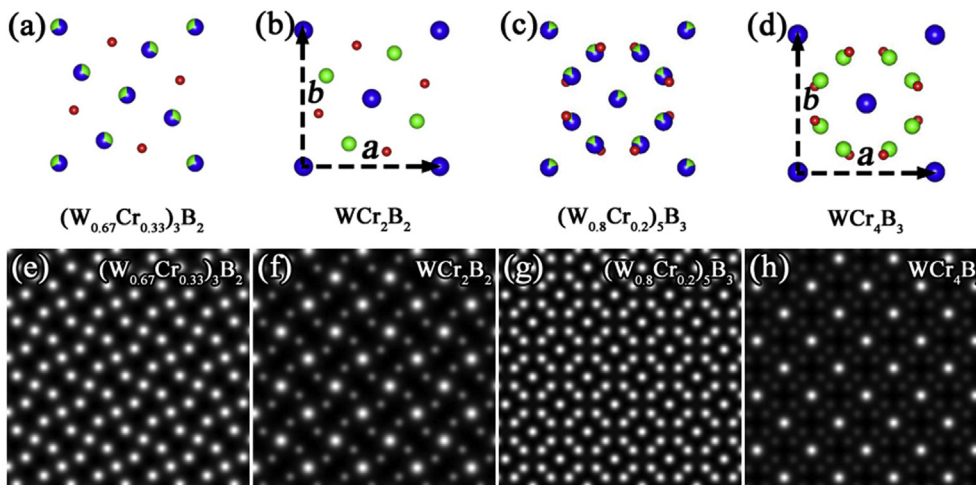


**Fig. 6.** Projections along [001] of hypothetical boride structures: (a) disordered  $(W_{0.67}Cr_{0.33})_3B_2$ , (b) ordered  $WCr_2B_2$ , (c) disordered  $(W_{0.8}Cr_{0.2})_5B_3$ , and (d) ordered  $WCr_4B_3$ . The small red balls, medium-sized green balls, and large blue balls represent B, Cr, and W atoms, respectively. Multicolored balls in (a) represent mixed W/Cr occupancy of  $4h$  and  $2a$  sites in the ratio 2:1. Multicolored balls in (c) represent mixed W/Cr occupancy of  $16l$  and  $4c$  sites in the ratio 4:1. Lattice vectors  $a$  and  $b$  in (c) and (g) are the same as in (a) and (e), respectively. (e), (f), (g) and (h): Simulated atomic resolution HAADF images of structures in (a), (b), (c), and (d), respectively, viewed down [001]. (For interpretation of the references to color in this figure legend, the reader is referred to the Web version of this article.)

**Table 2**Structure type, space group, lattice parameters, Wyckoff positions, and fractional atomic coordinates of ternary phases  $W_2CrB_2$  and  $W_4CrB_3$  obtained by calculation.

Compound	Space group	Structure type	Pearson symbol	Lattice parameters/Å	Atom (Wyckoff site)	Fractional coordinates		
						x	y	z
$W_2CrB_2$	$P4/mbm$	$V_3B_2$	$tP10$	$a = 5.824$ $c = 3.134$	W (4h)	0.1765	0.6765	0.5
					Cr (2a)	0.0	0.0	0.0
					B (4g)	0.3844	0.8844	0.0
$W_4CrB_3$	$I4/mcm$	$Cr_3B_3$	$tI32$	$a = 5.745$ $c = 10.951$	W (16l)	0.1706	0.6706	0.1443
					Cr (4c)	0.0	0.0	0.0
					B1 (8h)	0.6225	0.1225	0.0
					B2 (4a)	0.0	0.0	0.25

When rewritten as  $(W_3B_2)_{2/3} \cdot (Cr_3B_2)_{1/3}$ , and  $(W_3B_2)_{1/3} \cdot (Cr_3B_2)_{2/3}$ , respectively,  $W_2CrB_2$  and  $WCr_2B_2$  can be seen to belong to the pseudo-binary system  $W_3B_2$ - $Cr_3B_2$ . Their formation energies relative to the end-member phases were calculated to be  $-0.078$  eV/atom and  $+0.085$  eV/atom, respectively, showing that  $WCr_2B_2$  is much less stable than  $W_2CrB_2$ . These results are plotted in Fig. 7a, and explain why the experimentally observed phase is closer in composition to  $W_2CrB_2$  than  $WCr_2B_2$ .

To examine the tendency of transition metals to become ordered in this system, we used the USPEX code to generate the most A-site disordered structure of composition  $W_2CrB_2$  within a  $2 \times 2 \times 2$  supercell, corresponding to a generalized version of the special quasi-random structure, according to a procedure described elsewhere [47]. This structure was calculated to have a formation

energy of  $+0.029$  eV/atom relative to end members  $W_3B_2$  and  $Cr_3B_2$ ; as seen in Fig. 7a, the ordered form of  $W_2CrB_2$  is more thermodynamically stable than the disordered form by more than 0.1 eV/atom. Similarly, for the  $M_5B_3$  phase, within the pseudo-binary  $W_5B_3$ - $Cr_5B_3$  system, formation energies of ordered  $W_4CrB_3$ , disordered  $W_4CrB_3$ , and ordered  $WCr_4B_3$  were calculated to be  $-0.34$  eV/atom,  $+0.03$  eV/atom, and  $+0.38$  eV/atom, respectively. These results are summarized in Fig. 7b, and point towards ordered  $W_4CrB_3$  being the most stable phase.

Although the calculated formation energies of  $W_2CrB_2$  and  $W_4CrB_3$  are negative within their respective pseudo-binary systems, this does not necessarily mean they are thermodynamically stable in the W-Cr-B system as a whole. To confirm their overall stability we explored the W-Cr-B system in more detail. Based on

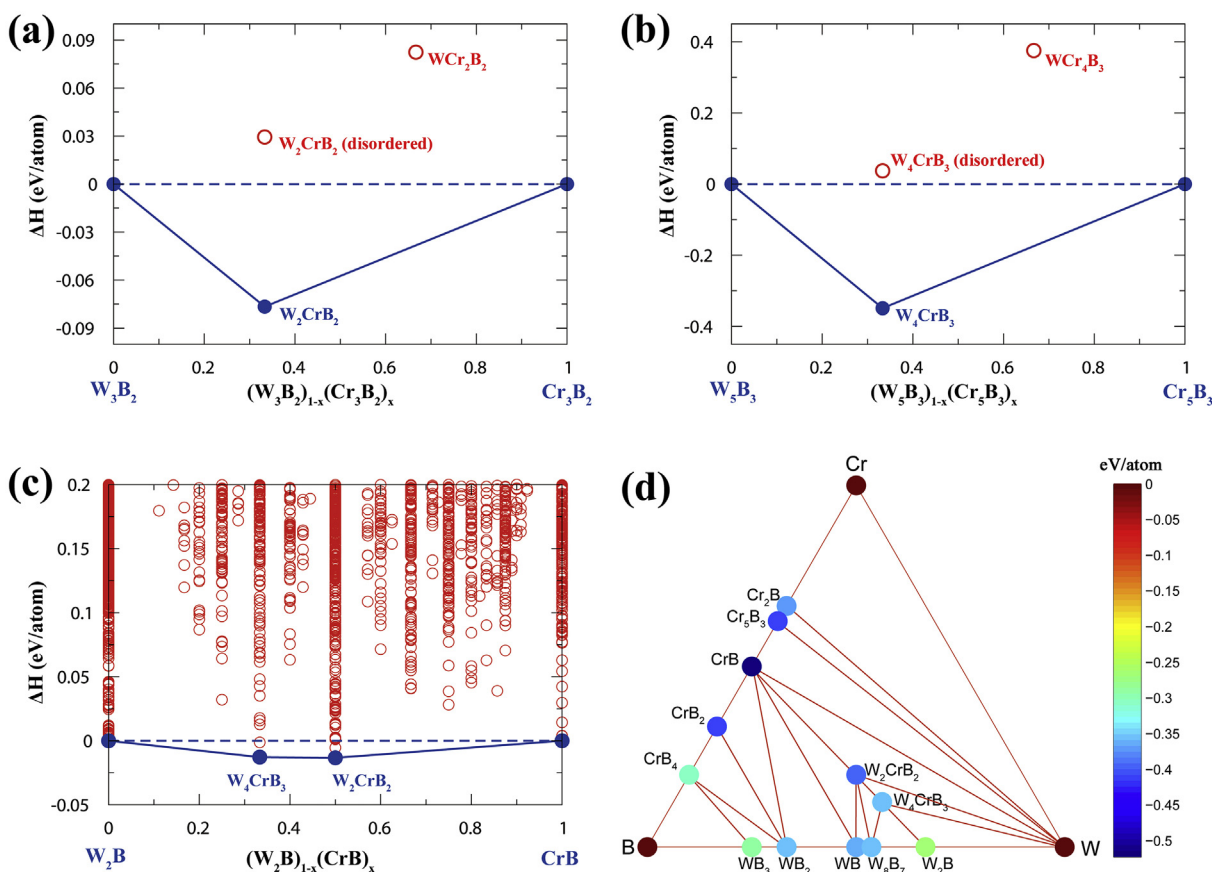


**Fig. 7.** Calculated enthalpies of formation of phases in (a)  $W_3B_2$ - $Cr_3B_2$ , (b)  $W_5B_3$ - $Cr_5B_3$ , and (c)  $W_2B$ - $CrB$  pseudo-binary systems. (d) Calculated ternary phase diagram for the W-Cr-B system showing formation energies color coded according to the scale bar on the right.  $W_3B_2$  and  $Cr_3B_2$  have the  $V_3B_2$  structure, and  $W_5B_3$  and  $Cr_5B_3$  have the  $Cr_3B_3$  structure. The ground-state structures of  $W_2B$ ,  $WB$ ,  $CrB$ , and  $Cr_2B$  are the same as reported in the literature [49,53]. Convex hulls were formed by connecting points corresponding to ground-state phases (blue circles). The convex hull of the  $W_2B$ - $CrB$  system was obtained by carrying out variable-composition crystal structure prediction, with each circle corresponding to a sampled structure. (For interpretation of the references to color in this figure legend, the reader is referred to the Web version of this article.)

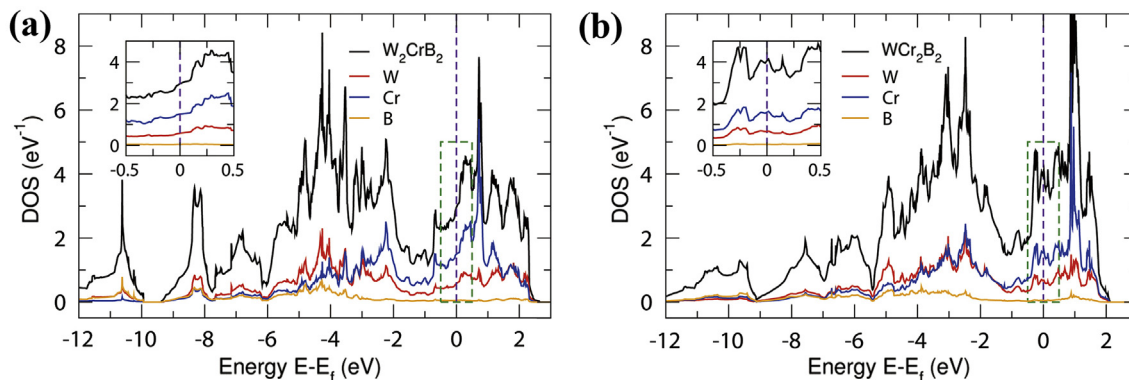


Fig. 8. Calculated densities of states (DOS) of (a)  $W_2CrB_2$  and (b)  $WCr_2B_2$ . Details around the Fermi level are shown in the inset.

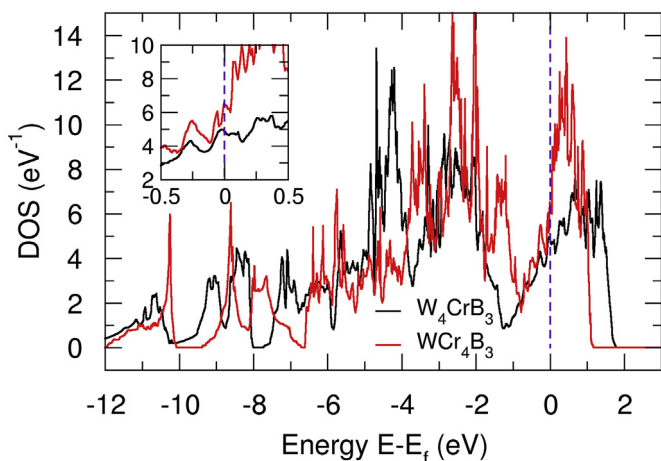


Fig. 9. Comparison of DOSs of ordered compounds  $W_4CrB_3$  and  $WCr_4B_3$ .

our USPEX simulations,  $W_2CrB_2$  and  $W_4CrB_3$  are both situated on the convex hull connecting end members  $W_2B$  and  $CrB$ , as shown in Fig. 7c. By taking into account all the known stable W-B [48] and Cr-B [49,50] compounds and calculating their ground-state energies with the VASP code, we derived their formation energies and

constructed the phase diagram shown in Fig. 7d. Both ternary  $W_2CrB_2$  and  $W_4CrB_3$  borides are seen to be thermodynamically stable within the W-Cr-B system.

The calculated electronic densities of states (DOSs) of  $W_2CrB_2$  and  $WCr_2B_2$  are compared in Fig. 8a and b. These show that both borides are metallic conductors and there is extensive electronic hybridization between the transition metal atoms and B. A pseudogap around the Fermi level can be observed in both phases. The DOS of  $WCr_2B_2$  at the Fermi level, located on the shoulder of the pseudogap, is much higher than that of  $W_2CrB_2$ , indicating lower energetic stability of  $WCr_2B_2$  compared with  $W_2CrB_2$ . Similar calculations for  $W_4CrB_3$  and  $WCr_4B_3$  revealed similar bonding characteristics, as shown in Fig. 9.  $W_4CrB_3$  is more stable than  $WCr_4B_3$  because of the lower DOS on the shoulder of the pseudogap.

Comparison of the crystal structures of  $W_2CrB_2$  and  $WCr_2B_2$  and their W-B and Cr-B bond lengths in Fig. 10a and b reveal interesting differences. Although Cr-B, (W-B)<sub>I</sub> and (W-B)<sub>II</sub> bonds in  $W_2CrB_2$  are similar in length, in  $WCr_2B_2$  the W-B and (Cr-B)<sub>II</sub> bonds are much longer than (Cr-B)<sub>I</sub> bonds. Bader analysis [51] gave an average charge of  $-0.9e$  for B in  $W_2CrB_2$  and  $-0.8e$  in  $WCr_2B_2$ . B atoms in  $W_2CrB_2$  thus have a higher electron density and are located in a more regular coordination environment than those in  $WCr_2B_2$ , which suggests the bonding in  $W_2CrB_2$  is (at least on average) stronger than that in  $WCr_2B_2$ , consistent with the greater stability of the former.

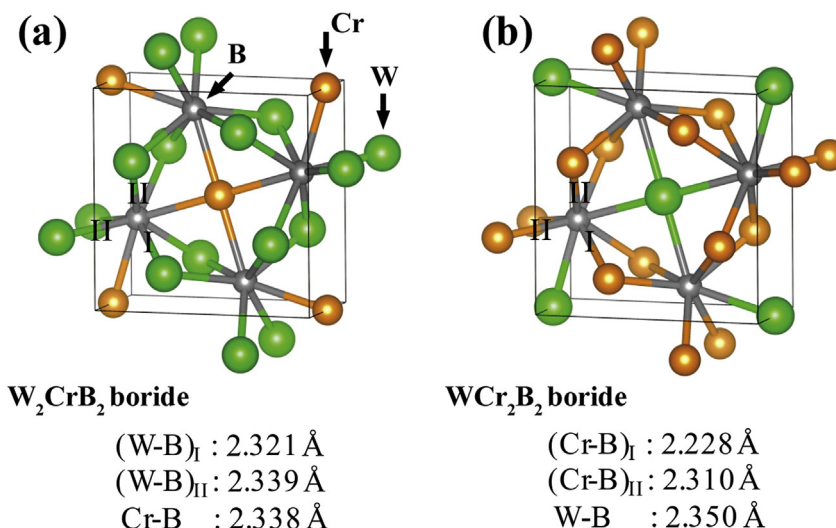


Fig. 10. Crystal structures of (a)  $W_2CrB_2$  and (b)  $WCr_2B_2$ . Chemical bonds Cr-B and W-B are highlighted.

**Table 3**Calculated elastic constants and mechanical properties (bulk modulus,  $B$ ; shear modulus,  $G$ ; Young's modulus,  $E$ ) of chemically ordered W-Cr-B compounds.

Compounds	$C_{11}$	$C_{33}$	$C_{44}$	$C_{66}$	$C_{12}$	$C_{13}$	$B$	$G$	$E$
$W_2CrB_2$	586.7	550.2	238.1	180.9	190.9	233.5	337.7	199.9	500.9
$WCr_2B_2$	579.1	510.6	177.4	120.6	189.3	187.1	310.1	166.4	423.5
$W_4CrB_3$	560.3	465.5	200.5	162.9	185.4	275.6	339.9	163.1	421.8
$WCr_4B_3$	549.3	508.9	178.2	151.1	155.5	169.4	288.4	175.1	436.8
$W_2B$	570.7	518.5	146.1	172.7	211.2	245.5	340.4	156.0	406.0
$Cr_2B$	521.1	493.3	206.5	201.0	179.8	197.4	298.3	185.3	460.6

Comparison of the calculated elastic properties and moduli of the various compounds, summarized in Table 3, supports this conclusion. The calculated bulk, shear, and Young's moduli of ordered  $W_2CrB_2$  are 337.7 GPa, 199.9 GPa, and 500.9 GPa, respectively, which are all higher than those of ordered  $WCr_2B_2$  at 310.1 GPa, 166.4 GPa, and 423.5 GPa, respectively, consistent with stronger bonding in  $W_2CrB_2$  than  $WCr_2B_2$ .

$W_4CrB_3$  and  $WCr_4B_3$  can be thought of as intergrowths of  $W_2CrB_2$  and  $W_2B$ , and  $WCr_2B_2$  and  $Cr_2B$ , respectively [25]. The bonding environments are thus more varied than in the case of  $W_2CrB_2$ , as reflected in the more complex relationship between their elastic properties: although their bulk moduli are very different, shear and Young's moduli are greater for  $WCr_4B_3$  than  $W_4CrB_3$ . This is likely related to the wide solid-solution range of  $(W,Cr)_5B_3$  reported by Telegus and Kuz'ma [52] for the  $Cr_5B_3$  ( $I4/mcm$ ) structured phase, and explains why ordering of W and Cr in  $M_5B_3$  is slightly weaker than in  $M_3B_2$ .

In addition, our calculations revealed that the molar volumes of the disordered phases are 1.5% and 1.2% larger than those of the ordered phases for  $W_2CrB_2$  and  $W_4CrB_3$ , respectively. This means the ordered phases are denser than their disordered forms, and hence their elastic properties should be greater because the averaged metal-boron bonds are shorter and stronger, which affects how the borides respond to lattice misfit and strain at precipitate/matrix interfaces. Ordered precipitates should thus act as stronger pinning centers than would be the case if the metal atoms were disordered, with greater resistance to dislocation motion across interfaces, and hence greater strength and creep resistance of the superalloys.

Similar chemical ordering phenomena to that observed in W-, Cr-, and Mo-rich borides in this study is also expected to occur in other multicomponent interstitial phases and precipitates (e.g., carbides, nitrides, and oxides) when metal atoms with very different atom sizes are involved. Characterization of new engineering alloys and reexamination of previously identified secondary phases using state-of-the-art techniques will likely provide new insights into their structures, stabilities, and properties. Applying this information to the design of engineering alloys is expected to result in the development of new materials of higher strength and greater performance.

#### 4. Conclusions

Atomic-resolution electron microscopy techniques were used to perform detailed structural analyses of  $M_3B_2$  and  $M_5B_3$  phases precipitated in the DAZ of a TLP-bonded superalloy.  $M_3B_2$  crystals were found to have  $P4/mbm$  symmetry, while  $M_5B_3$  crystals have  $I4/mcm$  symmetry. Distributions of different metal elements over two distinct lattice sites within the crystals of the two compounds were measured for the first time, and the stabilities of different metal configurations investigated using structure prediction methods based on a genetic algorithm. The main conclusions can be summarized as follows:

- 1) Chemical ordering of metal atoms on two distinct crystallographic sites in W/Cr-rich  $M_3B_2$  and  $M_5B_3$  crystals was observed, suggesting that they can more accurately be described as ternary borides than binary borides. Elements with larger atomic radii (e.g., W and Mo) preferentially occupy  $4h$  sites in  $M_3B_2$  and  $16l$  sites in  $M_5B_3$ , while elements with smaller atomic radii (e.g., Cr, Co, and Ni) preferentially occupy  $2a$  sites in  $M_3B_2$  and  $4c$  sites in  $M_5B_3$ . Using L to denote larger atoms and S to denote smaller atoms, the experimentally observed  $M_3B_2$  and  $M_5B_3$  phases can be written as  $L_2SB_2$  and  $L_4SB_3$ , respectively.
- 2) Systematic evaluation of possible phases in the W-Cr-B ternary system using theoretical methods showed that two previously unreported ternary phases,  $W_2CrB_2$  and  $W_4CrB_3$ , are more energetically stable than either of their disordered forms ( $(W,Cr)_3B_2$  and  $(W,Cr)_5B_3$ , respectively) or the inverse ordered forms  $WCr_2B_2$  and  $WCr_4B_3$ , respectively.
- 3) The observed chemical ordering of  $L_2SB_2$  and  $L_4SB_3$  in W/Cr-rich  $M_3B_2$  and  $M_5B_3$  precipitates is consistent with the computer modeling results showing that ordered forms  $W_2CrB_2$  and  $W_4CrB_3$  are more energetically favorable than the alternative forms. As the ordered forms are denser than the disordered forms, their mechanical properties are also expected to be greater.

#### Conflicts of interest

The authors declare no competing financial interests.

#### Acknowledgements

This work was financially supported by the National Natural Science Foundation of China under grant number 11327901 and the Russian Science Foundation under grant number 16-13-10459. A part of this work was conducted in the Research Hub for Advanced Nano Characterization, The University of Tokyo, as part of the "Nanotechnology Platform" (Project No.12024046) by MEXT, Japan. X.B. Hu thanks A. Kumamoto and B. Feng at the University of Tokyo for their support in operating the Dual SSD ARM.

#### References

- [1] Q.Z. Chen, N. Jones, D.M. Knowles, The microstructures of base/modified RR2072 SX superalloys and their effects on creep properties at elevated temperatures, *Acta Mater.* 50 (2002) 1095–1112.
- [2] J.C. Stinville, K. Gallup, T.M. Pollock, Transverse creep of Nickel-base superalloy bicrystals, *Metall. Mater. Trans. A* 46 (2015) 2516–2529.
- [3] P. Kontis, E. Alabort, D. Barba, D.M. Collins, A.J. Wilkinson, R.C. Reed, On the role of boron on improving ductility in a new polycrystalline superalloy, *Acta Mater.* 124 (2017) 489–500.
- [4] D. Tytko, P.-P. Choi, J. Klöwer, A. Kostka, G. Inden, D. Raabe, Microstructural evolution of a Ni-based superalloy (617B) at 700°C studied by electron microscopy and atom probe tomography, *Acta Mater.* 60 (2012) 1731–1740.
- [5] E. Cadel, D. Lemarchand, S. Chambréland, D. Blavette, Atom probe tomography investigation of the microstructure of superalloys N18, *Acta Mater.* 50 (2002) 957–966.
- [6] S. Antonov, J. Huo, Q. Feng, D. Iseim, D.N. Seidman, R.C. Helmink, E. Sun, S. Tin, The effect of Nb on grain boundary segregation of B in high refractory

- Ni-based superalloys, *Scripta Mater.* 138 (2017) 35–38.
- [7] H.R. Zhang, O.A. Ojo, M.C. Chaturvedi, Nanosize boride particles in heat-treated nickel base superalloys, *Scripta Mater.* 58 (2008) 167–170.
- [8] P. Kontis, H.A.M. Yusuf, S. Pedrazzini, M. Danaie, K.L. Moore, P.A.J. Bagot, M.P. Moody, C.R.M. Grovenor, R.C. Reed, On the effect of boron on grain boundary character in a new polycrystalline superalloy, *Acta Mater.* 103 (2016) 688–699.
- [9] X.B. Hu, L.Z. Zhou, J.S. Hou, X.Z. Qin, X.L. Ma, Interfacial precipitation of the  $M_5B_3$ -type boride in Ni-based superalloys, *Phil. Mag. Lett.* 96 (2016) 273–279.
- [10] P.A.J. Bagot, O.B.W. Silk, J.O. Douglas, S. Pedrazzini, D.J. Crudden, T.L. Martin, M.C. Hardy, M.P. Moody, R.C. Reed, An atom probe tomography study of site preference and partitioning in a nickel-based superalloy, *Acta Mater.* 125 (2017) 156–165.
- [11] M.J. Kaufman, V.I. Levit, Characterization of chromium boride precipitates in the commercial superalloy GTD 111 after long-term exposure, *Phil. Mag. Lett.* 88 (2008) 259–267.
- [12] X.B. Hu, Y.L. Zhu, X.L. Ma, Crystallographic account of nano-scaled intergrowth of  $M_2B$ -type borides in nickel-based superalloys, *Acta Mater.* 68 (2014) 70–81.
- [13] N.C. Sheng, J.D. Liu, T. Jin, X.F. Sun, Z.Q. Hu, Wide gap TLP bonding a single-crystal superalloy: evolution of the L/S interface morphology and formation of the isolated grain boundaries, *Metall. Mater. Trans. A* 44 (2013) 1793–1804.
- [14] M. Pouranvari, A. Ekrami, A.H. Kokabi, Microstructure–properties relationship of TLP-bonded GTD-111 nickel-base superalloy, *Mater. Sci. Eng. A* 490 (2008) 229–234.
- [15] S. Steuer, R.F. Singer, Boride zone formation in transient liquid phase bonding of pairings of parent superalloy materials with different compositions and grain structures, *Metall. Mater. Trans. A* 44 (2013) 2226–2232.
- [16] X.B. Hu, Y.L. Zhu, X.H. Shao, H.Y. Niu, L.Z. Zhou, X.L. Ma, Atomic configurations of various kinds of structural intergrowth in the polytypic  $M_2B$ -type boride precipitated in the Ni-based superalloy, *Acta Mater.* 100 (2015) 64–72.
- [17] Y.S. Zhao, Y.S. Zhao, J. Zhang, Y.S. Luo, G. Sha, D.Z. Tang, Q. Feng, Effect of Hf and B on transverse and longitudinal creep of a Re-containing nickel-base bicrystal superalloy, in: M. Hardy, E. Huron, U. Glatzel, B. Griffin, B. Lewis, C. Rae, V. Seetharaman, S. Tin (Eds.), *Superalloys 2016*, John Wiley & Sons Inc., New Jersey, 2016, pp. 683–692.
- [18] O.A. Idowu, O.A. Ojo, M.C. Chaturvedi, Microstructural study of transient liquid phase bonded cast INCONEL 738LC superalloy, *Metall. Mater. Trans. A* 37 (2006) 2787–2796.
- [19] H.J. Beattie, The crystal structure of an  $M_3B_2$ -type double boride, *Acta Crystallogr.* 11 (1958) 607–609.
- [20] P. Kontis, S. Pedrazzini, Y. Gong, P.A.J. Bagot, M.P. Moody, R.C. Reed, The effect of boron on oxide scale formation in a new polycrystalline superalloy, *Scripta Mater.* 127 (2017) 156–159.
- [21] B. Gault, M.P. Moody, F. De Geuser, A. La Fontaine, L.T. Stephenson, D. Haley, S.P. Ringer, Spatial resolution in atom probe tomography, *Microsc. Microanal.* 16 (2010) 99–110.
- [22] S. Meher, P. Nandwana, T. Rojhirunsakool, J. Tiley, R. Banerjee, Probing the crystallography of ordered Phases by coupling of orientation microscopy with atom probe tomography, *Ultramicroscopy* 148 (2015) 67–74.
- [23] S. Meher, T. Rojhirunsakool, P. Nandwana, J. Tiley, R. Banerjee, Determination of solute site occupancies within  $\gamma'$  precipitates in nickel-base superalloys via orientation-specific atom probe tomography, *Ultramicroscopy* 159 (2015) 272–277.
- [24] B. Gault, X.Y. Cui, M.P. Moody, F. De Geuser, C. Sigli, S.P. Ringer, A. Deschamps, Atom probe microscopy investigation of Mg site occupancy within  $\delta'$  precipitates in an Al–Mg–Li alloy, *Scripta Mater.* 66 (2012) 903–906.
- [25] X.B. Hu, Y.L. Zhu, N.C. Sheng, X.L. Ma, The Wyckoff positional order and polyhedral intergrowth in the  $M_3B_2$ - and  $M_5B_3$ -type boride precipitated in the Ni-based superalloys, *Sci. Rep.* 4 (2014) 7367.
- [26] K. Kimoto, T. Asaka, T. Nagai, M. Saito, Y. Matsui, K. Ishizuka, Element-selective imaging of atomic columns in a crystal using STEM and EELS, *Nature* 450 (2007) 702–704.
- [27] D.A. Muller, L.F. Kourkoutis, M. Murfitt, J.H. Song, H.Y. Hwang, J. Silcox, N. Dellby, O.L. Krivanek, Atomic-scale chemical imaging of composition and bonding by aberration-corrected microscopy, *Science* 319 (2008) 1073–1076.
- [28] M.W. Chu, S.C. Liou, C.P. Chang, F.S. Choa, C.H. Chen, Emergent chemical mapping at atomic-column resolution by energy-dispersive x-ray spectroscopy in an aberration-corrected electron microscope, *Phys. Rev. Lett.* 104 (2010) 196101.
- [29] L.J. Allen, A.J. D'Alfonso, B. Freitag, D.O. Klenov, Chemical mapping at atomic resolution using energy-dispersive x-ray spectroscopy, *MRS Bull.* 37 (2012) 47–52.
- [30] B. Feng, T. Yokoi, A. Kumamoto, M. Yoshiya, Y. Ikuhara, N. Shibata, Atomically ordered solute segregation behaviour in an oxide grain boundary, *Nat. Commun.* 7 (2016) 11079.
- [31] A. Kumamoto, N. Shibata, K. Nayuki, T. Tohei, N. Terasaki, Y. Nagatomo, T. Nagase, K. Akiyama, Y. Kuromitsu, Y. Ikuhara, Atomic structures of a liquid-phase bonded metal/nitride heterointerface, *Sci. Rep.* 6 (2016) 22936.
- [32] S. Wenner, L. Jones, C.D. Marioara, R. Holmestad, Atomic-resolution chemical mapping of ordered precipitates in Al alloys using energy-dispersive X-ray spectroscopy, *Micron* 96 (2017) 103–111.
- [33] C.W. Glass, A.R. Oganov, N. Hansen, USPEX–evolutionary crystal structure prediction, *Comput. Phys. Commun.* 175 (2006) 713–720.
- [34] A.R. Oganov, A.O. Lyakhov, M. Valle, How evolutionary crystal structure prediction works-and why, *Acc. Chem. Res.* 44 (2011) 227–237.
- [35] A.O. Lyakhov, A.R. Oganov, H.T. Stokes, Q. Zhu, New developments in evolutionary structure prediction algorithm USPEX, *Comput. Phys. Commun.* 184 (2013) 1172–1182.
- [36] N. Sheng, X. Hu, J. Liu, T. Jin, X. Sun, Z. Hu,  $M_3B_2$  and  $M_5B_3$  formation in diffusion-affected zone during transient liquid phase bonding single-crystal superalloys, *Metall. Mater. Trans. A* 46 (2015) 1670–1677.
- [37] R.F. Egerton, Electron energy-loss spectroscopy in the TEM, *Rep. Prog. Phys.* 72 (2009) 016502.
- [38] A.B. Riabov, V.A. Yartys, B.C. Hauback, P.W. Guegan, G. Wiesinger, I.R. Harris, Hydrogenation behaviour, neutron diffraction studies and microstructural characterisation of boron oxide-doped Zr–V alloys, *J. Alloy. Comp.* 293–295 (1999) 93–100.
- [39] H. Wu, W. Zhou, T.J. Udovic, J.J. Rush, T. Yildirim, Structural variations and hydrogen storage properties of  $Ca_5Si_3$  with  $Cr_3B_3$ -type structure, *Chem. Phys. Lett.* 460 (2008) 432–437.
- [40] Y.M. Ma, M. Eremets, A.R. Oganov, Y. Xie, I. Trojan, S. Medvedev, A.O. Lyakhov, M. Valle, V. Prakapenka, Transparent dense sodium, *Nature* 458 (2009) 182–U183.
- [41] W. Zhang, A.R. Oganov, A.F. Goncharov, Q. Zhu, S.E. Boulfelfel, A.O. Lyakhov, E. Stavrou, M. Somayazulu, V.B. Prakapenka, Z. Konopková, Unexpected stable stoichiometries of sodium chlorides, *Science* 342 (2013) 1502–1505.
- [42] G. Kresse, J. Furthmuller, Efficiency of ab-initio total energy calculations for metals and semiconductors using a plane-wave basis set, *Comput. Mater. Sci.* 6 (1996) 15–50.
- [43] G. Kresse, J. Furthmuller, Efficient iterative schemes for ab initio total-energy calculations using a plane-wave basis set, *Phys. Rev. B* 54 (1996) 11169–11186.
- [44] A. Togo, F. Oba, I. Tanaka, First-principles calculations of the ferroelastic transition between rutile-type and  $CaCl_2$ -type  $SiO_2$  at high pressures, *Phys. Rev. B* 78 (2008) 134106.
- [45] R. Hill, The elastic behaviour of a crystalline aggregate, *Proc. Phys. Soc. A* 65 (1952) 349.
- [46] S.J. Pennycook, D.E. Jesson, High-resolution Z-contrast imaging of crystals, *Ultramicroscopy* 37 (1991) 14–38.
- [47] A.R. Oganov, M. Valle, How to quantify energy landscapes of solids, *J. Chem. Phys.* 130 (2009) 104504.
- [48] X. Cheng, W. Zhang, X.-Q. Chen, H. Niu, P. Liu, K. Du, G. Liu, D. Li, H.-M. Cheng, H. Ye, Y. Li, Interstitial-boron solution strengthened  $WB_{3+x}$ , *Appl. Phys. Lett.* 103 (2013) 171903.
- [49] B. Wang, D.Y. Wang, Z. Cheng, X. Wang, Y.X. Wang, Phase stability and elastic properties of chromium borides with various stoichiometries, *ChemPhysChem* 14 (2013) 1245–1255.
- [50] H. Niu, J. Wang, X.-Q. Chen, D. Li, Y. Li, P. Lazar, R. Podloucky, A.N. Kolmogorov, Structure, bonding, and possible superhardness of  $CrB_4$ , *Phys. Rev. B* 85 (2012) 144116.
- [51] G. Henkelman, A. Arnaldsson, H. Jónsson, A fast and robust algorithm for Bader decomposition of charge density, *Comput. Mater. Sci.* 36 (2006) 354–360.
- [52] V.S. Telegus, Y.B. Kuz'ma, Phase equilibria in the systems tungsten–chromium–boron and tungsten–molybdenum–boron, *Powder Metall. Met. Ceram* 7 (1968) 133–138.
- [53] X.-Y. Cheng, X.-Q. Chen, D.-Z. Li, Y.-Y. Li, Computational materials discovery: the case of the W–B system, *Acta Crystallogr. C* 70 (2014) 85–103.